Carbon 183 (2021) 652–659

Contents lists available at ScienceDirect

Carbon

journal homepage: www.elsevier.com/locate/carbon

Hex-C_{558}: A new porous metallic carbon allotrope for lithium-ion battery anode

Keywords:
Porous metallic carbon
Lithium-ion battery anode
Specific capacity
Diffusion energy barrier
First-principles calculation

ABSTRACT

Due to the limited specific capacity of graphite anodes in lithium-ion batteries (LIBs), it is imperative to find alternatives with better performance. In this work, we propose, for the first time, a three dimensional (3D) porous metallic 5-5-8 carbon monolith with hexagonal lattice as a potential candidate. With 5-5-8 carbon nanoribbon as the building block, this material, named Hex-C_{558}, goes beyond graphene-nanoribbon-based 3D porous carbon structures. Using first-principles calculations, we show that Hex-C_{558} is not only dynamically and thermally stable, but also is energetically more favorable than many other theoretically predicted carbon allotropes. More importantly, Hex-C_{558} is metallic with ordered ionic conducting channels and possesses a low mass density of 1.05 gcm^{-3}, exhibiting great potential for ion-battery applications. As an anode for LIBs, Hex-C_{558} possesses a large specific capacity of 591 $mAhg^{-1}$, low diffusion energy barrier of 0.27 eV (at low Li concentration) and 0.52 eV (at high Li concentration), a low open-circuit voltage of 0.51 V, and a small volume change of 2.4%. This work provides a new route for the design and synthesis of novel carbon materials for battery applications by using pentagon-based building units.

1. Introduction

In the last three decades, tremendous efforts have been devoted to the study of carbon materials for lithium-ion batteries (LIBs) because of their unique advantages, such as availability, low cost, nontoxicity, and good reversibility for lithium intercalation and removal. Graphite has been the dominant active anode material used in LIBs since its commercialization in the early 1990s. However, the main problem of graphite anodes is its limited specific capacity (372 $mAhg^{-1}$), which cannot meet the requirements of economical and sustainable battery technologies for advanced electronic devices and vehicles. Thus, it is highly desirable to find new alternatives for LIB anode materials. To this end, porous materials for the anodes have received considerable attention because porous structures can provide more adsorption sites for Li-ions, which is favorable for achieving high capacity [1–4]. However, the conductivity and Coulombic efficiency of these materials synthesized in the laboratory have been found to be relatively low due to the disordered pores and structural defects [5,6]. Therefore, in recent years, many efforts have been devoted to studying porous metallic or semi-metallic carbon materials for overcoming such drawbacks [7–17]. For example, a graphene monolith (HZGM-42) [14] constructed by integrating zigzag graphene nanoribbons and sp^3-hybridized carbon chains shows topological semi-metallic feature and good performance for LIB anode with low Li diffusion energy barrier and high specific capacity that is 1.6 times as large as that of graphite.

Another class of carbon materials that have attracted increasing attention contain 5-5-8-units since the experimental observation of one-dimensional (1D) topological 5-5-8-defects in graphene [18]. Such defects can efficiently modulate the properties of carbon materials. For instance, it was found that the electronic structure and magnetic properties of armchair graphene nanoribbons can be effectively tuned by introducing 5–8 topological line defects [19]. The antiferromagnetic cross-edge coupling in zigzag graphene nanoribbons can be switched to ferromagnetic one when 5-5-8 defects are introduced [20]. More interestingly, it was found recently that a peanut-shaped carbon nanotube comprised of 5-5-8 units shows metallicity and low lattice thermal conductivity [21], very different from conventional carbon nanotubes. Although 2D carbon sheets composed of 5-5-8 units were proposed and found to be metallic or semi-metallic with high Fermi velocity for electrons [22], no studies have been reported on 3D carbon monoliths constructed by using 5-5-8 carbon nanoribbon as the building block, which may lead to metallic electronic structure and good performance when used an anode material for LIBs. This motivated us to carry out this study.

In this work, using state-of-the-art theoretical methods, we propose a hexagonal 5-5-8 carbon monolith, Hex-C_{558}, and systematically study its stability, electronic properties, and the performance as an anode material in LIBs. We show that Hex-C_{558} is a promising candidate for LIB anodes.

2. Computational methods

First-principles calculations based on density functional theory (DFT) are performed by using Vienna *Ab initio* Simulation Package

https://doi.org/10.1016/j.carbon.2021.07.045

(VASP) [23] with the projector augmented wave potential [24]. The exchange and correlation interactions between electrons are treated by using the Perdew-Burke-Ernzerhof functional (PBE) [25] within the generalized gradient approximation (GGA) [26]. The Heyd-Scuseria-Ernzerhof hybrid functional (HSE06) [27] is used to obtain more accurate electronic band structure. The plane-wave energy cutoff is set to 800 eV for all the calculations. For geometry optimization, the convergence criteria for the total energy and force are set at 10^{-8} eV and 10^{-6} eVÅ^{-1}, respectively. The 3 × 3 × 7 Monkhorst-Pack *k*-meshes are used to sample the first Brillouin zone [28]. *Ab initio* molecular dynamics (AIMD) simulations are carried out to verify the thermal stability with the canonical ensemble. The temperature is controlled by using the Nosé thermostat [29]. The dynamic stability is confirmed by phonon spectrum, which is calculated by using the finite displacement method [30] implemented in the Phonopy code [31]. A tight-binding (TB) Hamiltonian is constructed by projecting the Bloch states onto the maximally localized Wannier functions using the WANNIER90 package [32]. The diffusion energy barriers for Li-ions are calculated by using the climbing-image nudged elastic band (CI-NEB) method [33]. The effect of van der Waals interaction during the adsorption and diffusion of Li-ions is considered by using the PBE-D2 functional that contains the semi-empirical long-range dispersion correction [34].

3. Results and discussion

3.1. Structure and stability

This carbon allotrope is constructed by using 5-5-8 carbon nanoribbons and the ethane molecules as the possible precursors (Fig. 1(a)). Connecting the three 5-5-8 carbon nanoribbons together through carbon dimers via dehydrogenation of ethane (Fig. 1(b)) results in a 3D porous structure, as plotted in Fig. 1(c). It is encouraging to note that 3D porous graphene composed of graphene nanoribbons has been successfully synthesized [35], and the 1D topological 5-5-8-defects have been observed in graphene [18]. Based on these advances, thus, it is reasonable to expect that Hex-C_{558} can be synthesized by introducing 5-5-8-defects into 3D porous graphene. The optimized structure has hexagonal symmetry with space group *P6mm*; thus we name it Hex-C_{558}. The unit cell of Hex-C_{558} contains 34 atoms with the lattice constants of $a = b = 12.43$ Å, $c = 4.82$ Å. In this structure, there are eight chemically nonequivalent carbon atoms, occupying the Wyckoff positions of $6e_1$ (0.438, 0.562, 0.381), $6e_2$ (0.434, 0.566, 0.867), $6e_3$ (0.405, 0.595, 0.130), $6e_4$ (0.400, 0.600, 0.616), $3c_1$ (0.500, 0.500, 0.775), $3c_2$ (0.500, 0.500, 0.483), $2b_1$ (0.667, 0.333, 0.200), and $2b_2$ (0.667, 0.333, 0.538), respectively. Hex-C_{558} possesses large 1D hexagonal channels with a diameter of 14.3 Å, as shown in Fig. 1(c). This is larger than that of the ordered hexagonal channels in hC28 (11.8 Å) [11] and C-h (10.4 Å) [13]. Moreover, due to its porosity, Hex-C_{558} has a low mass density of 1.05 gcm^{-3}, which is even lower than that of the recently reported low density carbon anode, BDL-14 (1.41 gcm^{-3}) [9].

The energetic stability of Hex-C_{558} is studied by calculating its total energy as a function of the volume. The calculations are also performed for some other stable carbon allotropes for comparison, including diamond, graphite, T6-carbon [36], Tri-C_9 [37], K6-carbon [38], and H_{18}-carbon [39]. As shown in Fig. 2(a), except for graphite and diamond, Hex-C_{558} has the lowest energy among them, implying a good possibility for its experimental realization. Next, the dynamical stability of Hex-C_{558} is examined by calculating the phonon spectrum as given in Fig. 2(b). The absence of imaginary vibrational modes demonstrates the dynamic stability of this structure. In addition, we calculate the group velocities of the acoustic branches near the Γ point along the Γ-M path by using formula $\mathbf{v}_g(\mathbf{q}) = \nabla_{\mathbf{q}} w(\mathbf{q})$, while the group velocities of diamond are also calculated as comparsion. The group velocities of Hex-C_{558} are found to be 2.0, 8.3, and 10.6 km s^{-1} for the three acoustic branches, respectively, which are all considerably lower than those of diamond near the Γ point along the Γ-X path (11.6, 12.8, and 18.1 km s^{-1}). However, the metallic feature of Hex-C_{558} makes the electronic thermal conductivity dominant, namely, Hex-C_{558} remains highly thermally conductive.

Next, the thermal stability is studied by performing AIMD simulations at temperatures ranging from 300 K to 1200 K using a supercell of 1 × 1 × 3. The duration of the simulated heating processes is 8 ps with a time step of 1 fs. As shown in Fig. 2(c), the total potential energy fluctuates around a constant, and the atomic configuration of Hex-C_{558} remains almost intact during the entire

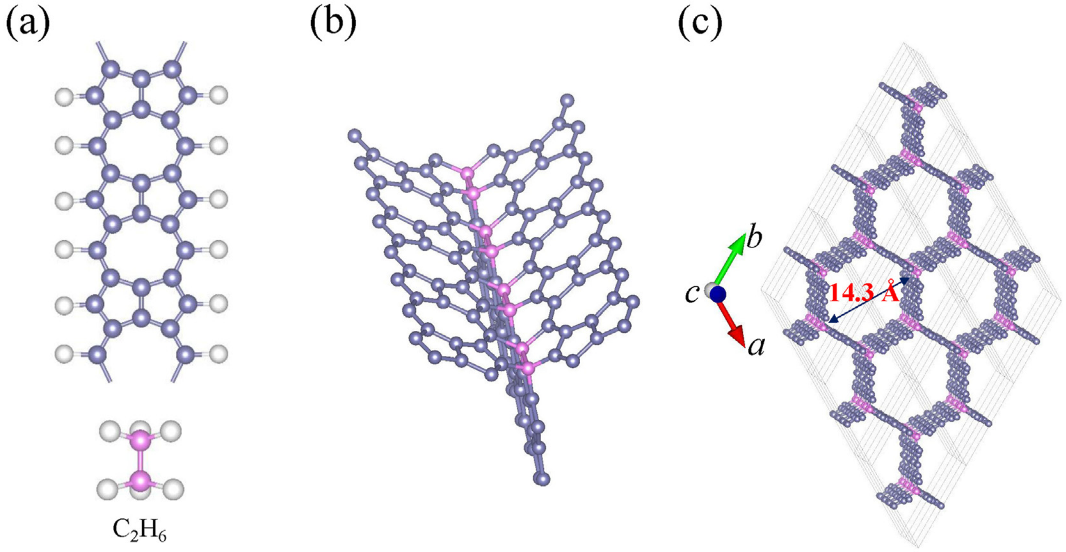

Fig. 1. (a) Possible precursors (5-5-8 carbon nanoribbon and ethane molecule), (b) perspective view of three 5-5-8 nanoribbons linked with C_2 units, and (c) perspective view of optimized geometry of Hex-C_{558}. The gray and pink spheres represent the sp^2-and sp^3-hybridized carbon atoms, respectively. (A colour version of this figure can be viewed online.)

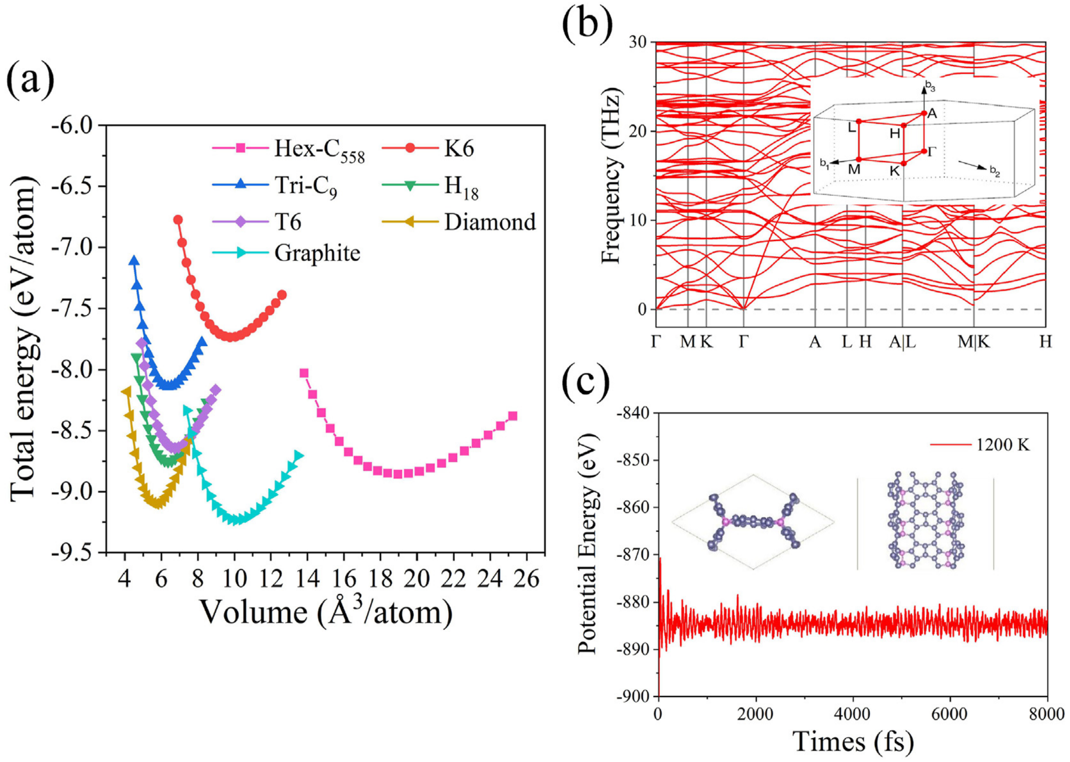

Fig. 2. (a) Variation of the energy per atom of Hex-C_{558} and some other carbon allotropes with respect to volume. (b) Phonon spectrum of Hex-C_{558} along the high symmetry q-point path in the first Brillouin zone. (c) Total potential energy fluctuation during AIMD simulation at 1200 K. The insets are the top and side views of the Hex-C_{558} structure at the end of the simulation at 1200 K.

simulation at 1200 K, confirming the thermal stability of Hex-C_{558}. In addition, using AIMD simulations, we have also confirmed its thermal stability under humid conditions at 300 K by adding a few H_2O molecules in the $1 \times 1 \times 3$ supercell of Hex-C_{558}, as shown in Fig. S1.

The mechanical stability is examined by using the Born-Huang criteria [40]. For a hexagonal lattice, there are five independent elastic constants that can be calculated using the energy-strain method implemented in AELAS software [41]. The calculated elastic constants are $C_{11} = 125.9$ GPa, $C_{12} = 119.7$ GPa, $C_{13} = 38.0$ GPa, $C_{33} = 420.4$ GPa, and $C_{44} = 68.1$ GPa, which fully satisfy the Born-Huang criteria, namely, $C_{44} > 0$, $C_{11} > |C_{12}|$, $(C_{11}+C_{12})\ C_{33} > 2C_{13}^2$, demonstrating that Hex-C_{558} is mechanically stable.

3.2. Mechanical properties

Based on the elastic constants of Hex-C_{558}, we calculate its Young's modulus (Y) by using the following formula [42]:

$$Y(\boldsymbol{n}) = \frac{1}{s_{11}(1-n_3^2)^2 + s_{33}n_3^4 + (2s_{13}+s_{44})(1-n_3^2)n_3^2} \qquad (1)$$

where s_{11}, s_{13}, s_{33}, and s_{44} are elastic compliance coefficients, $\boldsymbol{n}=(n_1, n_2, n_3)$ is a unit vector along the stretching direction. The calculated Young's moduli of Hex-C_{558} for the different directions are listed in Table 1. One can see that the Young's modulus along the $\boldsymbol{c}$ direction is much larger than that along the $\boldsymbol{a}$ and $\boldsymbol{b}$ directions, showing a highly mechanical anisotropy. The calculations are also carried out for HZGM-42 [14] and hC28 [11] that possess hexagonal lattices as well, but have the 6-membered rings as their building units. From Table 1, we note that the Young's moduli of Hex-C_{558} are significantly smaller than those of HZGM-42 and hC28, suggesting that the 5-5-8 structure is softer and more elastic than the two structures composed of the hexagonal units.

Table 1
Calculated elastic constants (C_{ij} in GPa) and Young's moduli (Y in GPa) for Hex-C_{558}, and for other two hexagonal carbon allotropes HZGM-42 and hC28.

	Hex-C_{558}	HZGM-42	hC28
C_{11}	125.9	198.0	157.5
C_{12}	119.7	86.5	147.9
C_{13}	38.0	56.3	47.7
C_{33}	420.4	637.7	591.4
C_{44}	68.1	138.4	103.5
$Y(\boldsymbol{a})$	12.1	158.6	18.6
$Y(\boldsymbol{b})$	12.1	158.6	18.6
$Y(\boldsymbol{c})$	408.6	615.4	576.5

Next, to examine the maximum tensile strength of Hex-C_{558}, we use the deformation with a small increment of 0.01 to realize the quasi-static displacement-controlled deformation in the x, y, and z direction, respectively. The comparison of results for different cell size is given in Fig. S2, suggesting that the cell size that we used for calculation is appropriate. The calculated stress-strain curves along the different axes are plotted in Fig. 3, where the fracture strain for Hex-C_{558} under loading is 0.30, 0.33, and 0.18 along the x, y, and z direction, respectively, which are comparable to the corresponding values of 0.32, 0.31, and 0.18 for hC28 that is composed of graphene nanoribbons with the hexagonal building unit [11].

3.3. Electronic properties

To study the electronic properties of Hex-C_{558}, we first calculate its band structure at the PBE level. As shown in Fig. 4(a), Hex-C_{558} is

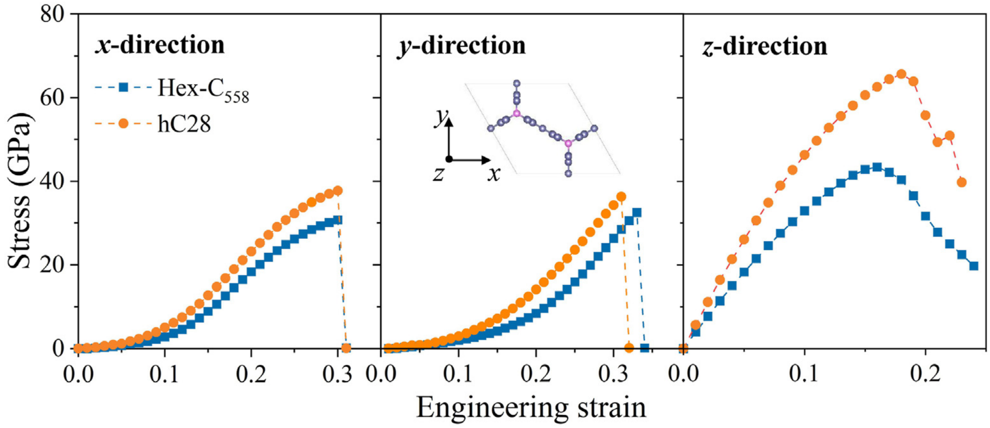

Fig. 3. Variation of the stress with tensile strain along the x, y, and z direction for Hex-C_{558} and hC28.

metallic because the partially occupied energy bands cross the Fermi level along the Γ-M, K-Γ, and Γ-A paths. To further confirm the metallicity of Hex-C_{558}, the band structure is recalculated by using the more accurate hybridized functional of HSE06 [27], as given in Fig. 4(a), indicating that the metallic feature of Hex-C_{558} is secured. We then calculate the partial density of states (PDOS) projected on the sp^2-and sp^3-hybridized carbon atoms and the partial charge density around the Fermi level from −0.5 to 0.5 eV. The results are plotted in Fig. 4(a and b), showing that the bands near the Fermi level mainly originate from the sp^2-hybridized carbon atoms that make up the pentagons in 5-5-8 nanoribbons. To identify the electron delocalization and electron conducting channels, we further calculate the electron localization function (ELF) of Hex-C_{558}. ELF has been widely used to describe the electron distribution in materials [43–45], which takes the values between 0 and 1. Here, 0 corresponds to very low charge density [46], 1 represents

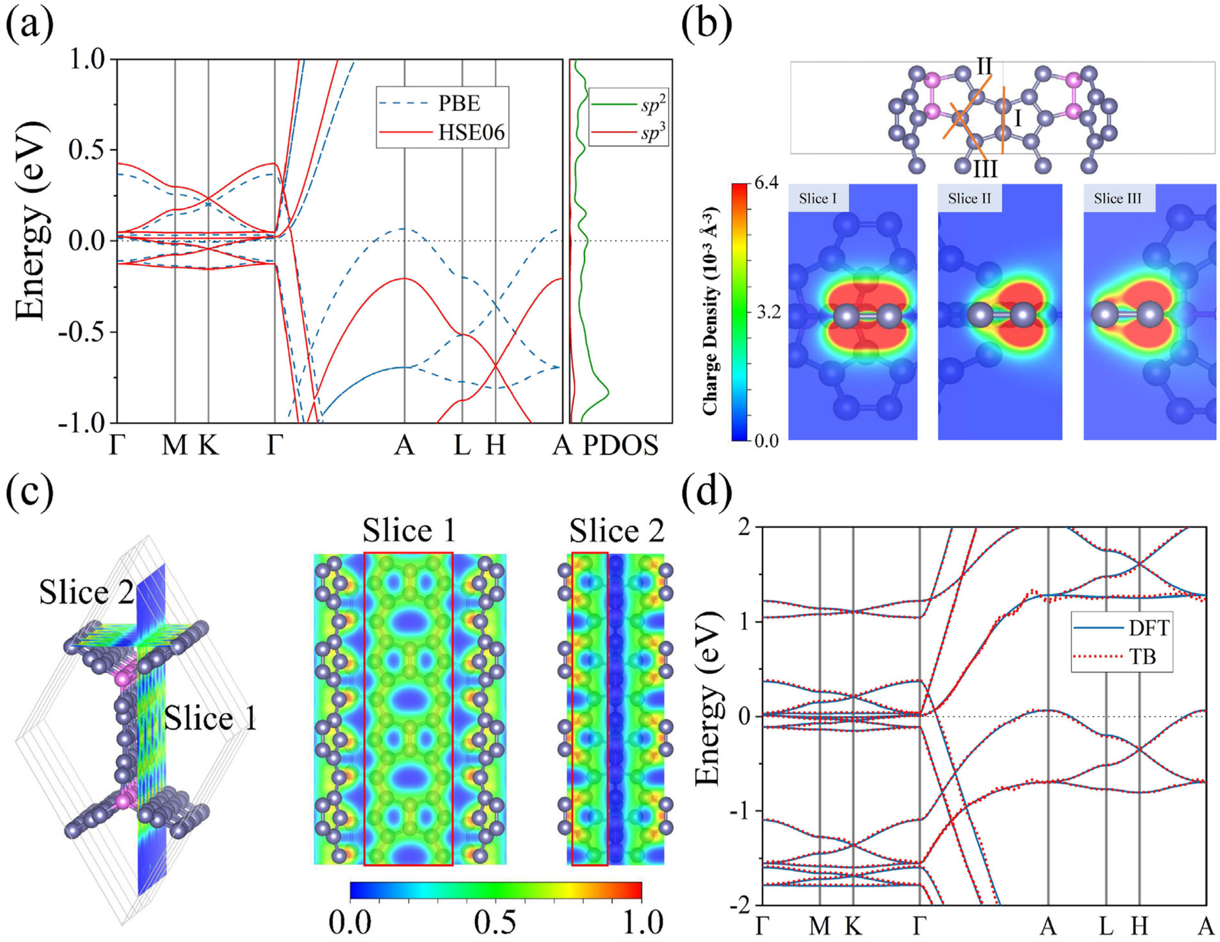

Fig. 4. (a) Electronic band structures at the PBE and HSE06 levels, and projected DOS for the sp^2-and sp^3-hybridized carbon atoms. (b) Top and side views of the partial charge density near the Fermi level from −0.5 to 0.5 eV. (c) ELF distribution on the two slices of Hex-C_{558}. (d) TB-band structure in comparison with that of DFT for Hex-C_{558}.

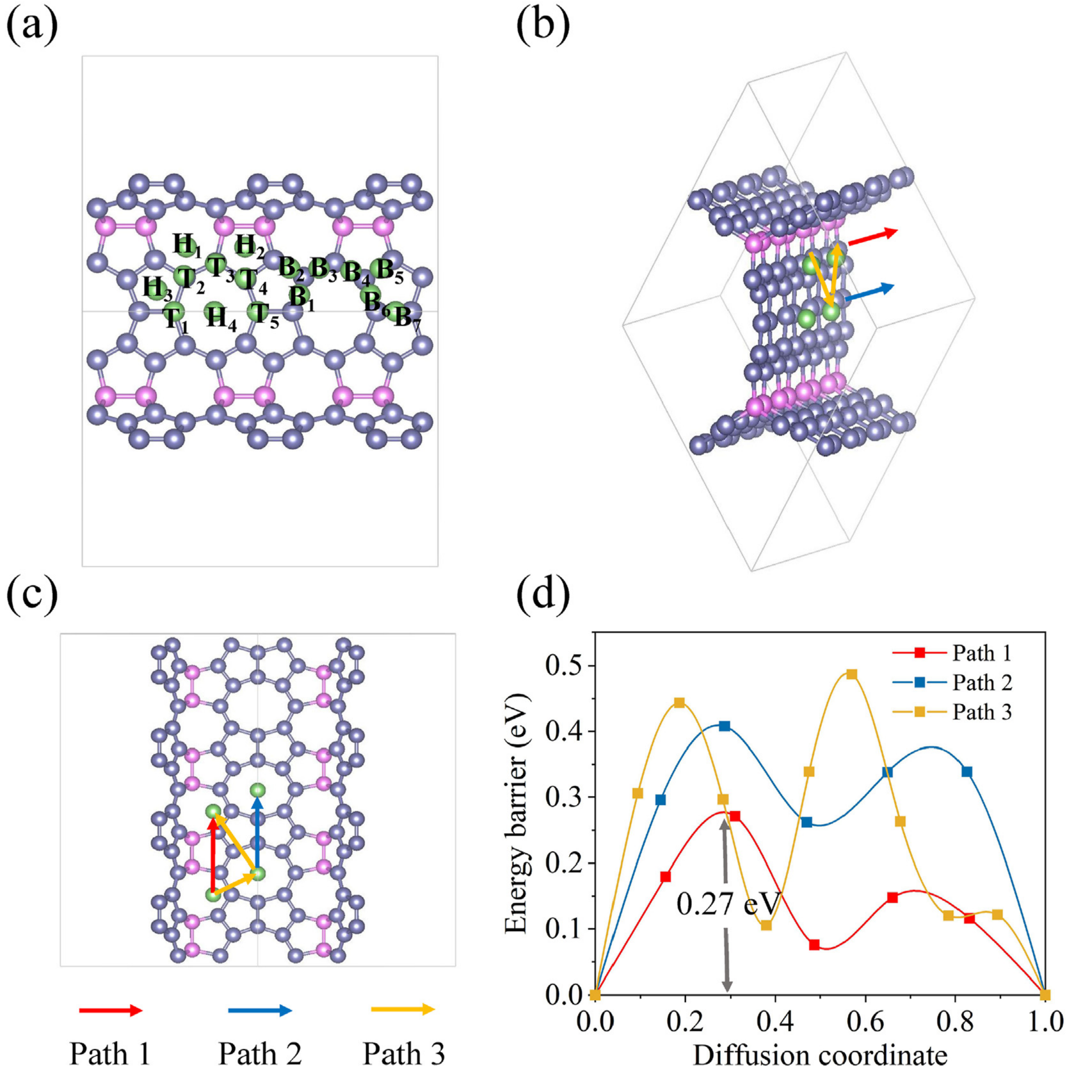

Fig. 5. (a) Side view of all possible single Li-ion adsorption sites in Hex-C_{558}. (b) Perspective view and (c) side view of the possible paths for Li-ion diffusions along the conducting channels. (d) Diffusion energy barriers for the three paths. The gray, pink, and green spheres represent sp^2-, sp^3-hybridized carbon atoms, and Li ions, respectively. (A colour version of this figure can be viewed online.)

the fully localized electrons and 0.5 refers to the fully delocalized electrons. As shown in Fig. 4(c), the regions highlighted by the red rectangles correspond to the delocalized channel of electrons.

To further verify the orbital composition around the Fermi level, TB model is then used. Based on the dumbbell-shaped partial charge density distributed on the slices shown in Fig. 4(b), we can reasonably expect that the orbitals near the Fermi level are mainly contributed from the p_z-orbitals of the sp^2-hybridized carbon atoms. Accordingly, we use the p_z-orbitals of these carbon atoms to construct the TB Hamiltonian:

$$H = \varepsilon_0 \sum_i c_i^\dagger c_i + \sum_{ij} (t_{ij} c_i^\dagger c_j + H.c.). \tag{2}$$

where $c_i^\dagger$ and c_i are the electronic creation and annihilation operators of the p_z-orbital at site i, respectively, ε_0 is the on-site energy, and t_{ij} is the hopping integral for describing the jumping process of electrons from one site to another. The band structure reproduced by using the TB model is plotted in Fig. 4(d), which agrees well with the results of DFT-based calculations, further confirming that the exhibited metallicity in Hex-C_{558} mainly comes from the p_z-orbitals of the sp^2 carbon atoms that form the pentagons in the 5-5-8 nanoribbons, as shown in Fig. 4(b).

3.4. Application as an anode material for LIBs

Considering the special geometry with regular large pores and intrinsic metallicity, Hex-C_{558} could offer more binding sites and efficient diffusion channels for Li ions, and provide the basis for the storage and transportation of Li ions with good conductivity. Hence, we study its applications as an anode material for LIBs. We first examine the stable adsorption sites. To avoid interactions between the periodic images of Li ions, a 1 × 1 × 4 supercell of Hex-C_{558} is used in the calculations. The stability of adsorption is examined by the binding energy E_b, defined as

$$E_b = (E_{Li_x-Hex-C_{558}} - E_{Hex-C_{558}} - x\mu_{Li})/x \tag{3}$$

where $E_{Lix\text{-}Hex\text{-}C558}$ and $E_{Hex\text{-}C558}$ are the total energies of Li-intercalated and non-intercalated configurations, respectively, μ_{Li} is the energy of one Li atom in its bulk phase, and x is the number of Li atoms in the supercell. As shown in Fig. 5(a), sixteen possible

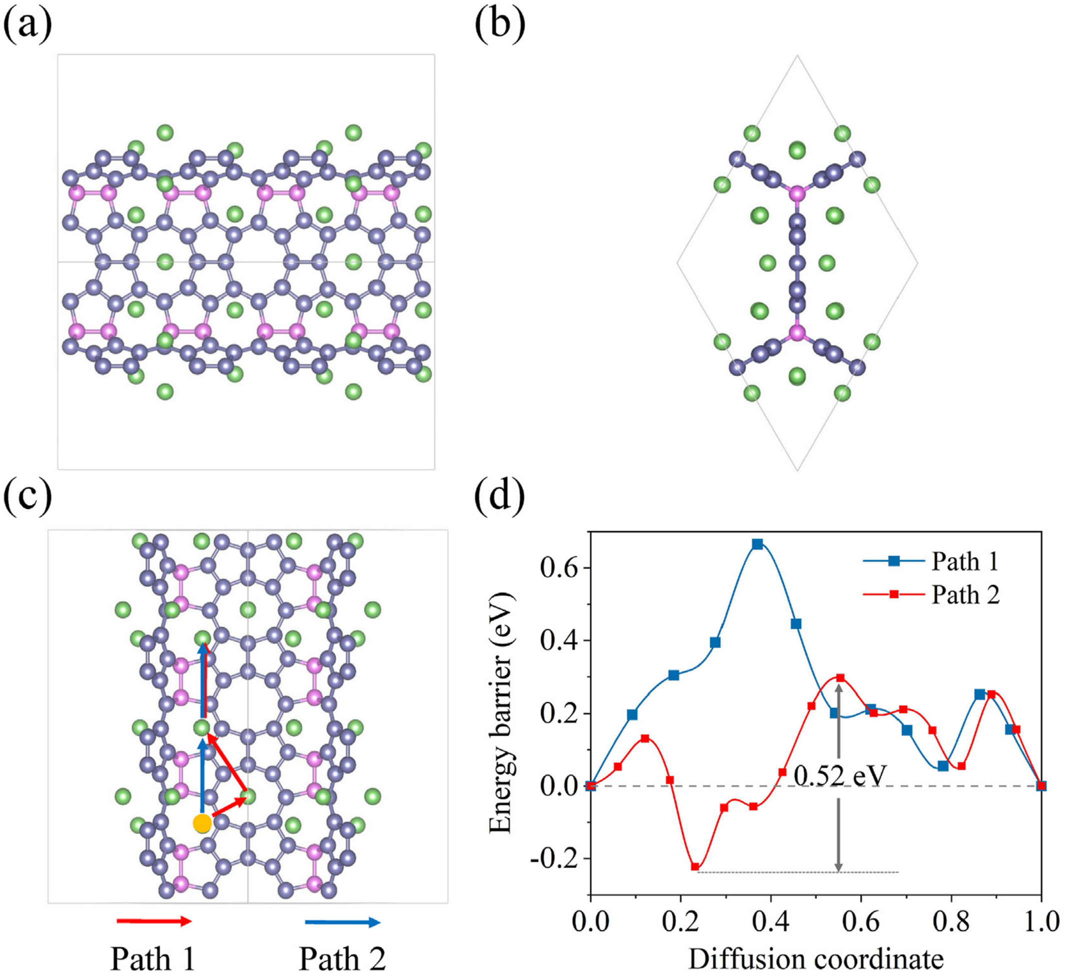

Fig. 6. (a) Side view and (b) top view of the fully Li-intercalated Hex-C_{558}. (c) Migration paths for the vacancy diffusion. (d) Energy profile of Path 1 and Path 2. The yellow sphere in (c) represents the vacancy. (A colour version of this figure can be viewed online.)

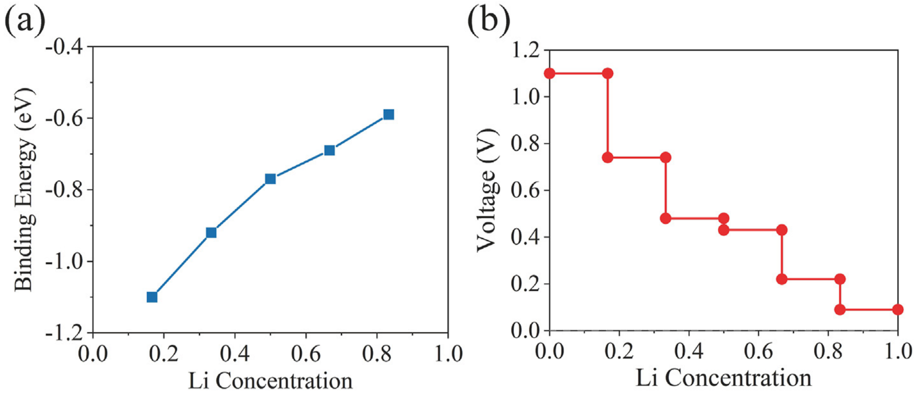

Fig. 7. (a) Binding energy of five configurations with intermediate Li-concentration, and (b) voltage profile of Hex-C_{558} in the half-cell.

symmetry-nonequivalent adsorption sites are studied, including four hollow sites (above the centers of the different carbon rings), labeled as H_1, H_2, H_3, and H_4, five top sites labeled as T_1 toT_5, and seven bridge sites, i.e., B_1 to B_7. After geometric optimization, five stable adsorption sites are identified, which are H_1, H_2, H_3, H_4, and B_7. The corresponding binding energies are calculated to be 1.09, 1.02, 0.99, 0.98, and 0.73 eV, respectively. Next, the Bader charge analysis [47] is performed for studying the charge transfer from Li ions on these adsorption sites. The results show that 0.88 and 0.90 electrons are transferred from Li atoms to the substrate for H_1, H_2, H_3 sites and H_4, B_7 sites, respectively, indicating the strong Coulomb interactions between the Li ions and Hex-C_{558}.

In addition to the electronic conductivity that is confirmed by the metallic band structure, the ion conductivity is also required for high-rate capability of batteries. Therefore, we study the diffusion process of Li ions. Due to the symmetry constraints, we find

Table 2
Performance comparison of Hex-C_{558} with some other carbon allotropes used for anode materials in LIBs.

Materials	Density (gcm^{-3})	Reversible capacity ($mAhg^{-1}$)	Diffusion barrier (eV)	OCV (V)	Volume change (%)	Electronic property
Hex-C_{558}	1.05	591	0.27	0.51	2.4	Metallic
graphite [7,14]	2.24	372	0.22–0.40	0.11	10.0	Metallic
IGN [15]	2.61	298	0.01	0.66	3.2	Semimetallic
bco-C_{16} [10]	2.58	558	0.53	0.23	13.4	Semimetallic
Immm-C16 [17]	2.04	558	0.01	0.40	2.9	Semimetallic
Hex-C_{18} [7]	2.41	496	0.02–0.14	–	–	Metallic
HZGM-42 [14]	1.39	425	0.02	0.50	2.4	Semimetallic
m-C_{16} [16]	2.31	558	0.25	0.56	3.6	Semimetallic

that there are three possible paths in Hex-C_{558} for Li-ion diffusion along the conducting channels at low Li concentration (LiC_{136}), as shown in Fig. 5(b and c). Path 1 and Path 2 are the straightforward paths as the Li ions move along the channel, while Path 3 requires hopping from one adsorption site to another. The calculated energy barriers are plotted in Fig. 5(d), showing that the migration path with the lowest energy barrier is Path 1, which has an energy barrier of 0.27 eV, lower than that in bco-C_{16} (0.53 eV) [10].

Next, we study the maximum specific capacity of Hex-C_{558}. We gradually increase Li concentration until the full Li-intercalation in Hex-C_{558} is reached, as shown in Fig. 6(a and b). In this configuration, all of H_1 sites and half of H_4 sites are occupied. The corresponding theoretical specific capacity is 591 $mAhg^{-1}$, larger than that of many carbon anodes, including graphite (372 $mAhg^{-1}$), bco-C_{16} (558 $mAhg^{-1}$) [10], and IGN (372 $mAhg^{-1}$) [15].

To investigate the Li-ion migration at high Li concentration, we remove one Li ion from the fully Li-intercalated Hex-C_{558} configuration and examine the diffusion energy barrier of the vacancy by using the CI-NEB method [33]. There are two possible migration paths for the vacancy diffusion, as shown in Fig. 6(c). Path 1 represents the straightforward migration of vacancies, while Path 2 is for the hopping between the nonequivalent sites. The migration energy barriers are plotted in Fig. 6(d), indicating that the energy barrier of the vacancy along Path 2 is 0.52 eV, which is lower than 0.67 eV along Path 1, suggesting that Path 2 is more favorable for the migration of Li ions at high Li concentration.

We further study the performance of Hex-C_{558} as an anode by calculating the open-circuit voltage (OCV) using the following formula,

$$V \approx -\frac{E_{Li_{x_2}-Hex-C_{558}} - E_{Li_{x_1}-Hex-C_{558}} - (x_2 - x_1)\mu_{Li}}{(x_2 - x_1)e} \tag{4}$$

where $E_{Lix2\text{-}Hex\text{-}C558}$, $E_{Lix1\text{-}Hex\text{-}C558}$, and μ_{Li} are the total energies of x_2-, x_1-intercalated Hex-C_{558} and one Li atom in Li bulk, respectively. To obtain the total energy at different Li concentrations, we examine five intermediate adsorption concentrations, i.e., $Li_xC_{3.78}$, $x = 0.167$, 0.333, 0.500, 0.667, and 0.833, corresponding to the adsorption configurations of Li_6C_{136}, $Li_{12}C_{136}$, $Li_{18}C_{136}$ $Li_{24}C_{136}$ and $Li_{30}C_{136}$, respectively, and calculate 12 nonequivalent configurations for each Li concentration. All the intermediate configurations are generated by comparing the electrostatic Ewald energy of the symmetry-nonequivalent structures as implemented in the pymatgen package [48,49]. The binding energies for the most stable configurations at each intermediate concentration are shown in Fig. 7(a), while the corresponding voltage profile is plotted in Fig. 7(b). One can see that the voltage is positive through the whole voltage profile, suggesting a reversible capacity of 591 $mAhg^{-1}$. The average OCV is calculated to be 0.51 V, which is lower than that of IGN (0.66 V) [15], m-C_{16} (0.56 V) [16], and comparable to that of HZGM-42 (0.50 V) [14].

To examine the cycling stability, we calculate the volume change of the fully Li–intercalated Hex-C_{558} and pristine Hex-C_{558} using the formula: $\Delta V = \frac{V_{Li} - V_0}{V_0} \times 100\%$. Here, V_{Li} and V_0 are the volumes of the fully and none Li-intercalated Hex-C_{558} configurations, respectively. The calculated volume expansion is 2.4% without bond breaking, which is smaller than that of graphite (10.0%), bco-C_{16} (13.4%) [10], and IGN (3.2%) [15], indicating that Hex-C_{558} as an anode material for LIBs exhibits good cycling stability.

For clarity, we summarize the six key quantities of Hex-C_{558} for LIB anode applications in Table 2. The corresponding parameters for some other recently studied carbon anode materials are also listed for comparison. It shows that Hex-C_{558} possesses the lowest density, the largest reversible capacity, and the smallest volume change among these carbon anodes.

4. Conclusions

In summary, based on first-principles calculations, we propose a new 3D porous carbon monolith by connecting the zigzag edged 5-5-8 carbon nanoribbons with carbon dimers via dehydrogenation of the ethane molecules. We term this new material Hex-C_{558}. Although it is metastable compared to graphite and diamond, is energetically more favorable than many other carbon allotropes. Further, it can withstand high temperatures up to 1200 K and has low mass density and high mechanical anisotropy. Hex-C_{558} is metallic and possesses electronic conducting channels along the z direction. The TB model analysis reveals that the metallicity comes from the p_z-orbitals of the sp^2 hybridized carbon atoms that form the pentagons in 5-5-8 nanoribbons. As an anode material for LIBs, Hex-C_{558} exhibits a large specific capacity of 591 $mAhg^{-1}$, low ionic diffusion energy barrier of 0.27 and 0.52 eV for the low and high Li concentration, respectively, low OCV of 0.51 V, and a small volume change of 2.4%. These properties suggest that Hex-C_{558} is a promising anode material and 5-5-8 structural units can be used for the design of new carbon materials with new features.

Declaration of competing interest

The authors declare that they have no known competing financial interests or personal relationships that could have appeared to influence the work reported in this paper.

Acknowledgments

This work is partially supported by grants from the National Natural Science Foundation of China (Grant Nos: NSFC-11974028 and NSFC-21773004), the National Key Research and Development Program of the Ministry of Science and Technology of China (2017YFA0205003), and is supported by the High-Performance Computing Platform of Peking University, China. P. J. acknowledges partial support by the U.S DOE, Office of Basic Energy Sciences, Division of Material Sciences and Engineering under Award No. DE-FG02-96ER45579. D. N. thanks Dr. Xiaoyin Li for helpful discussions. The authors thank the crew of the Center for Computational Materials Science, the Institute for Materials Research, Tohoku

University (Japan), for their continuous support of the MASAMUNE-IMR supercomputing facility.

Appendix A. Supplementary data

Supplementary data to this article can be found online at https://doi.org/10.1016/j.carbon.2021.07.045.

References

[1] B. Xing, H. Zeng, G. Huang, C. Zhang, R. Yuan, Y. Cao, et al., Porous graphene prepared from anthracite as high performance anode materials for lithium-ion battery applications, J. Alloys Compd. 779 (2019) 202.

[2] R. Dash, S. Pannala, Retracted article: theoretical limits of energy density in silicon-carbon composite anode based lithium ion batteries, Sci. Rep. 6 (2016) 27449.

[3] M. Ge, J. Rong, X. Fang, C. Zhou, Porous doped silicon nanowires for lithium ion battery anode with long cycle life, Nano Lett. 12 (2012) 2318.

[4] J. Ma, J. Sung, J. Hong, S. Chae, N. Kim, S.-H. Choi, et al., Towards maximized volumetric capacity via pore-coordinated design for large-volume-change lithium-ion battery anodes, Nat. Commun. 10 (2019) 475.

[5] A.T. Tesfaye, R. Gonzalez, J.L. Coffer, T. Djenizian, Porous silicon nanotube arrays as anode material for Li-ion batteries, ACS Appl. Mater. Interfaces 7 (2015) 20495.

[6] H. He, D. Sun, Y. Tang, H. Wang, M. Shao, Understanding and improving the initial Coulombic efficiency of high-capacity anode materials for practical sodium ion batteries, Energy Storage Materials 23 (2019) 233.

[7] J. Liu, T. Zhao, S. Zhang, Q. Wang, A new metallic carbon allotrope with high stability and potential for lithium ion battery anode material, Nanomater. Energy 38 (2017) 263.

[8] Y. Qie, J. Liu, S. Wang, Q. Sun, P. Jena, Tetragonal C_{24}: a topological nodal-surface semimetal with potential as an anode material for sodium ion batteries, J. Mater. Chem. 7 (2019) 5733.

[9] X. Li, J. Liu, F.Q. Wang, Q. Wang, P. Jena, Rational design of porous nodal-line semimetallic carbon for K-ion battery anode materials, J. Phys. Chem. Lett. 10 (2019) 6360.

[10] J. Liu, S. Wang, Q. Sun, All-carbon-based porous topological semimetal for Li-ion battery anode material, Proc. Natl. Acad. Sci. Unit. States Am. 114 (2017) 651.

[11] J. Hu, W. Wu, C. Zhong, N. Liu, C. Ouyang, H.Y. Yang, et al., Three-dimensional honeycomb carbon: junction line distortion and novel emergent fermions, Carbon 141 (2019) 417.

[12] W. Zhou, H. Xie, S. Wang, Q. Wang, P. Jena, A 3D porous honeycomb carbon as Na-ion battery anode material with high capacity, excellent rate performance, and robust stability, Carbon 168 (2020) 163.

[13] L. Shi, A. Xu, T. Zhao, Three-dimensional carbon-honeycomb as nanoporous lithium and sodium deposition scaffold, J. Phys. Chem. C 122 (2018) 21262.

[14] J. Liu, X. Li, Q. Wang, Y. Kawazoe, P. Jena, A new 3D Dirac nodal-line semi-metallic graphene monolith for lithium ion battery anode materials, J. Mater. Chem. 6 (2018) 13816.

[15] J. Liu, S. Wang, Y. Qie, C. Zhang, Q. Sun, High-pressure-assisted design of porous topological semimetal carbon for Li-ion battery anode with high-rate performance, Physical Review Materials 2 (2018), 025403.

[16] H. Xie, Y. Qie, M. Imran, Q. Sun, Topological semimetal porous carbon as a high-performance anode for Li-ion batteries, J. Mater. Chem. 7 (2019) 14253.

[17] S. Wang, B. Yang, Dirac nodal line semimetal of three-dimensional cross-linked graphene network as anode materials for Li-ion battery beyond graphite, ACS Appl. Energy Mater. 4 (2021) 2091.

[18] J. Lahiri, Y. Lin, P. Bozkurt, I.I. Oleynik, M. Batzill, An extended defect in graphene as a metallic wire, Nat. Nanotechnol. 5 (2010) 326.

[19] Q.Q. Dai, Y.F. Zhu, Q. Jiang, Electronic and magnetic properties of armchair graphene nanoribbons with 558 grain boundary, Phys. Chem. Chem. Phys. 16 (2014) 10607.

[20] X. Lin, J. Ni, Half-metallicity in graphene nanoribbons with topological line defects, Phys. Rev. B 84 (2011), 075461.

[21] J. Sun, Y. Chen, Q. Wang, Low lattice thermal conductivity of a 5-8-peanut-shaped carbon nanotube, Phys. Chem. Chem. Phys. 23 (2021) 5460.

[22] C. Su, H. Jiang, J. Feng, Two-dimensional carbon allotrope with strong electronic anisotropy, Phys. Rev. B 87 (2013), 075453.

[23] G. Kresse, J. Furthmüller, Efficient iterative schemes for ab initio total-energy calculations using a plane-wave basis set, Phys. Rev. B 54 (1996) 11169.

[24] P.E. Blöchl, Projector augmented-wave method, Phys. Rev. B 50 (1994) 17953.

[25] J.P. Perdew, K. Burke, M. Ernzerhof, Generalized gradient approximation made simple, Phys. Rev. Lett. 77 (1996) 3865.

[26] M.P. Teter, M.C. Payne, D.C. Allan, Solution of Schrödinger's equation for large systems, Phys. Rev. B 40 (1989) 12255.

[27] J. Heyd, G.E. Scuseria, M. Ernzerhof, Hybrid functionals based on a screened Coulomb potential, J. Chem. Phys. 118 (2003) 8207.

[28] H.J. Monkhorst, J.D. Pack, Special points for Brillouin-zone integrations, Phys. Rev. B 13 (1976) 5188.

[29] S. Nosé, A unified formulation of the constant temperature molecular dynamics methods, J. Chem. Phys. 81 (1984) 511.

[30] K. Parlinski, Z.Q. Li, Y. Kawazoe, First-principles determination of the soft mode in cubic ZrO_2, Phys. Rev. Lett. 78 (1997) 4063.

[31] A. Togo, F. Oba, I. Tanaka, First-principles calculations of the ferroelastic transition between rutile-type and $CaCl_2$-type SiO_2 at high pressures, Phys. Rev. B 78 (2008) 134106.

[32] A.A. Mostofi, J.R. Yates, Y.-S. Lee, I. Souza, D. Vanderbilt, N. Marzari, Wannier90: a tool for obtaining maximally-localised Wannier functions, Comput. Phys. Commun. 178 (2008) 685.

[33] G. Mills, H. Jónsson, Quantum and thermal effects in H_2 dissociative adsorption: evaluation of free energy barriers in multidimensional quantum systems, Phys. Rev. Lett. 72 (1994) 1124.

[34] S. Grimme, Semiempirical GGA-type density functional constructed with a long-range dispersion correction, J. Comput. Chem. 27 (2006) 1787.

[35] N.V. Krainyukova, E.N. Zubarev, Carbon honeycomb high capacity storage for gaseous and liquid species, Phys. Rev. Lett. 116 (2016), 055501.

[36] S. Zhang, Q. Wang, X. Chen, P. Jena, Stable three-dimensional metallic carbon with interlocking hexagons, Proc. Natl. Acad. Sci. Unit. States Am. 110 (2013) 18809.

[37] Y. Cheng, R. Melnik, Y. Kawazoe, B. Wen, Three dimensional metallic carbon from distorting sp^3-bond, Cryst. Growth Des. 16 (2016) 1360.

[38] C.-Y. Niu, X.-Q. Wang, J.-T. Wang, K6 carbon: a metallic carbon allotrope in sp^3 bonding networks, J. Chem. Phys. 140 (2014), 054514.

[39] C.-X. Zhao, C.-Y. Niu, Z.-J. Qin, X.Y. Ren, J.-T. Wang, J.-H. Cho, et al., H_{18} carbon: a new metallic phase with sp^2-sp^3 hybridized bonding network, Sci. Rep. 6 (2016) 21879.

[40] Z.-j. Wu, E.-j. Zhao, H.-p. Xiang, X.-f. Hao, X.-j. Liu, J. Meng, Crystal structures and elastic properties of superhard IrN_2 and IrN_3 from first principles, Phys. Rev. B 76 (2007), 054115.

[41] S.H. Zhang, R.F. Zhang, AELAS: automatic ELAStic property derivations via high-throughput first-principles computation, Comput. Phys. Commun. 220 (2017) 403.

[42] V.A. Gorodtsov, D.S. Lisovenko, Extreme values of Young's modulus and Poisson's ratio of hexagonal crystals, Mech. Mater. 134 (2019) 1.

[43] A. Savin, A.D. Becke, J. Flad, R. Nesper, H. Preuss, H.G. von Schnering, A new look at electron localization, Angew Chem. Int. Ed. Engl. 30 (1991) 409.

[44] B. Silvi, A. Savin, Classification of chemical bonds based on topological analysis of electron localization functions, Nature 371 (1994) 683.

[45] A. Savin, O. Jepsen, J. Flad, O.K. Andersen, H. Preuss, H.G. von Schnering, Electron localization in solid-state structures of the elements: the diamond structure, Angew Chem. Int. Ed. Engl. 31 (1992) 187.

[46] A.D. Becke, K.E. Edgecombe, A simple measure of electron localization in atomic and molecular systems, J. Chem. Phys. 92 (1990) 5397.

[47] W. Tang, E. Sanville, G. Henkelman, A grid-based Bader analysis algorithm without lattice bias, J. Phys. Condens. Matter 21 (2009), 084204.

[48] S.P. Ong, W.D. Richards, A. Jain, G. Hautier, M. Kocher, S. Cholia, et al., Python Materials Genomics (pymatgen): a robust, open-source python library for materials analysis, Comput. Mater. Sci. 68 (2013) 314.

[49] S. Wang, Q. Bai, A.M. Nolan, Y. Liu, S. Gong, Q. Sun, et al., Lithium chlorides and bromides as promising solid-state chemistries for fast ion conductors with good electrochemical stability, Angew. Chem. Int. Ed. 58 (2019) 8039.

Dongyuan Ni, Yiheng Shen, Yupeng Shen, Qian Wang[*]
School of Materials Science and Engineering, BKL-MEMD, Peking University, Beijing, China

Center for Applied Physics and Technology, HEDPS, College of Engineering, Peking University, Beijing, 100871, China

Y. Kawazoe
New Industry Creation Hatchery Center, Tohoku University, Sendai, 980-8577, Japan

Department of Physics, Suranaree University of Technology, Nakhon Ratchasima, Thailand

Department of Physics and Nanotechnology, SRM Institute of Science and Technology, 50 Kattankulathur, Tamil Nadu, 603203, India

Puru Jena
Department of Physics, Virginia Commonwealth University, Richmond, VA, 23284, USA

[*] Corresponding author.
E-mail address: qianwang2@pku.edu.cn (Q. Wang).

9 May 2021
Available online 20 July 2021